Absolute differential cross sections for the scattering of kilo-electron-volt O atoms

G. J. Smith, R. S. Gao, B. G. Lindsay, K. A. Smith, and R. F. Stebbings
Department of Physics, Department of Space Physics and Astronomy
and Rice Quantum Institute, Rice University, Post Office Box 1892, Houston, Texas 77251
(Received 2 October 1995)

This paper reports measurements of absolute differential cross sections for the direct scattering of oxygen atoms by He, Ne, Ar, Kr, Xe, H_2, N_2, O_2, CO, CO_2, H_2O, SO_2, NH_3, CH_4, CF_4, and SF_6 targets. The measured cross sections include contributions from all elastic and inelastic processes that result in a fast neutral oxygen atom product. Cross sections are presented for 0.5- and 1.5-keV projectile energies over the laboratory angular range 0.2°–5°. When compared in the center-of-mass reference frame, these cross sections exhibit a high degree of similarity in both amplitude and angular dependence. The cross sections for N_2, CO, CO_2, and H_2O are inverted using a partial-wave analysis to yield empirical interaction potentials, which can then be used to extrapolate the measurements down to lower energies. Using these potentials, cross sections are evaluated at 0.1 keV.

PACS number(s): 34.50.Lf, 34.20.−b

I. INTRODUCTION

Measurements of differential scattering cross sections involving fast oxygen atoms are of continuing interest to both experimentalists and theorists due to their importance in a wide range of environments. In the earth's atmosphere, significant fluxes of precipitating O^+ ring-current ions have been observed from altitudes of around 200 to 1000 km during geomagnetic storms [1–3]. With energies ranging from a few hundred to several thousand eV, these fast ions undergo charge transfer collisions with thermospheric atomic hydrogen and oxygen producing fast neutral oxygen atoms. Through subsequent collisions including elastic scattering, collisional excitation, and collisional ionization, these atoms transfer their kinetic energy to the atmosphere, resulting in local heating and optical emissions. Similarly, collisions involving fast oxygen atoms play a significant role in other environments including the important area of fusion research [4]. While measurements of atomic oxygen scattering from a limited number of targets have been previously reported [5], an extension of this work to include a wider range of targets and extrapolation to lower collision energies is presented here in an effort to aid researchers in the accurate modeling of these environments.

II. APPARATUS AND EXPERIMENTAL METHOD

A schematic of the apparatus, which has been previously described in detail [6,7], is shown in Fig. 1. Briefly, oxygen ions are produced through electron impact on CO_2 in a magnetically confined plasma. Ions effusing from the ion source are accelerated to the desired beam energy and focused by a three element electrostatic lens. The resulting beam is momentum analyzed by a pair of bending magnets, and the O^+ component is directed through a charge-transfer cell (CTC) where a small fraction is converted to fast neutral oxygen atoms through charge-transfer collisions with N_2. It has been previously argued that the neutral beam would be composed primarily of ground-state atoms produced

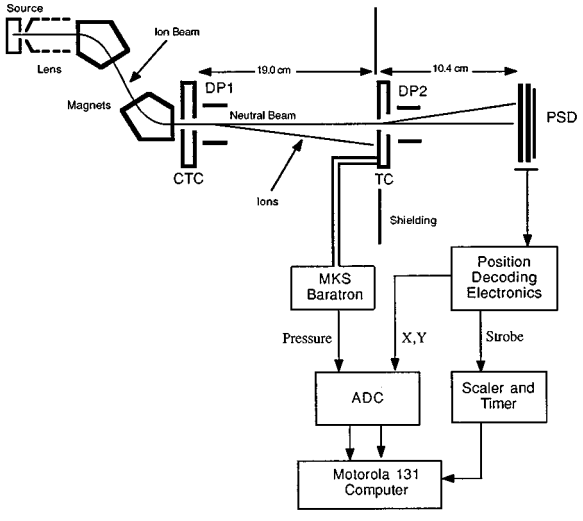

FIG. 1. Schematic of the apparatus.

TABLE I. Experimental uncertainties.

Experimental quantity	Uncertainty
Cross-section amplitude uncertainties	
Counting statistics	3–20 %
(Primary beam)/(Scattered signal) detection efficiency	3%
TC length l	2%
TC pressure (number density n)	2%
Baratron thermal transpiration	2%
Cross-section angular uncertainties	
TC to PSD distance	1%
Beam divergence	0.015°
Analysis ring width	0.035°–0.140°
PSD position encoding error	0.035° [7]
PSD linearity	2%

 © 1996 The American Physical Society

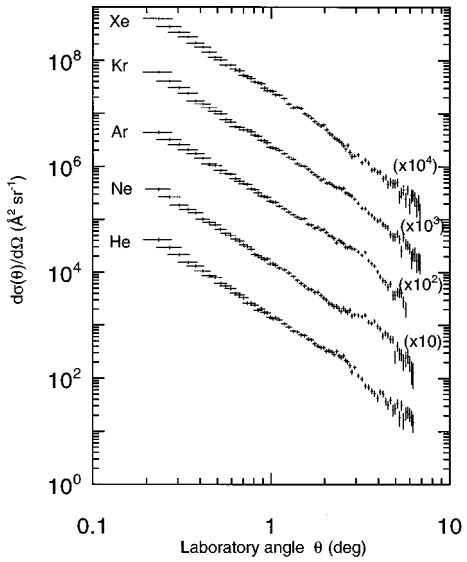

FIG. 2. Differential cross sections for elastic scattering of 0.5 keV O atoms by He, Ne, Ar, Kr, and Xe. The cross sections have been multiplied by the factors indicated.

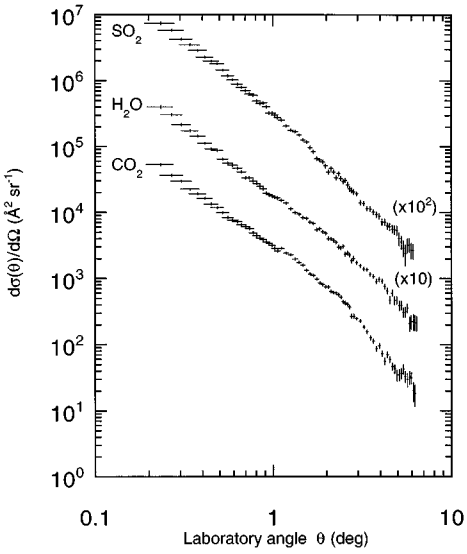

FIG. 4. Differential cross sections for elastic scattering of 0.5 keV O atoms by CO_2, H_2O, and SO_2. The cross sections have been multiplied by the factors indicated.

through the near-resonant reaction channel $O^+(^2D)+N_2 \rightarrow O(^3P)\ N_2^+(A^2\Pi_u)$ [8,9]; however, the direct-scattering cross sections are found to be insensitive to the state of the incident atoms through measurements carried out using a mixed-state O beam produced through O^+ + Kr charge transfer. The neutral beam is then collimated to within 0.015° divergence by two laser drilled apertures (50 μm diam.) defining the exit of the CTC and the entrance of the target cell (TC). Electrostatic deflection plates DP1 between the apertures remove residual ions from the beam. A gas target is introduced into the TC with a typical pressure of approximately 4 mtorr, and as the target cell length is 1.6 mm only a small percentage (1–4 %) of the primary beam is scattered. Under these thin target conditions effects due to secondary collisions are avoided. Both primary beam atoms and scattered atoms exiting the TC are detected with a position-sensitive detector (PSD). This detector, which has been previously described in detail [10], consists of two microchannel plates stacked in a chevron configuration mounted above a resistive anode. When a particle strikes the first microchannel plate a cascade of secondary electrons is produced that is further amplified by the second plate and the resultant charge is collected on the resistive anode. By measuring the relative magnitudes of the current pulses at the four corners of the anode, one can accurately locate the centroid of this charge distribution and hence the point of impact

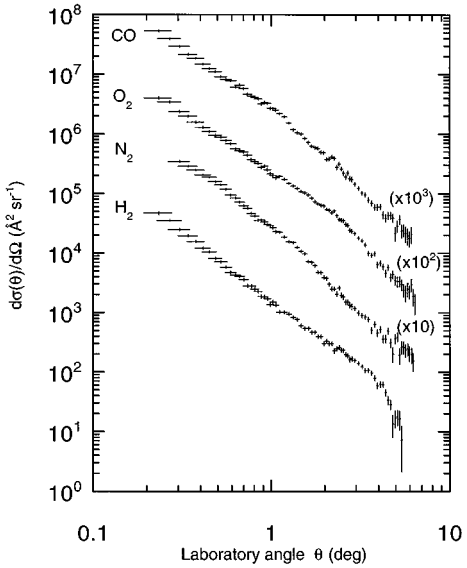

FIG. 3. Differential cross sections for elastic scattering of 0.5 keV O atoms by H_2, N_2, O_2, and CO. The cross sections have been multiplied by the factors indicated.

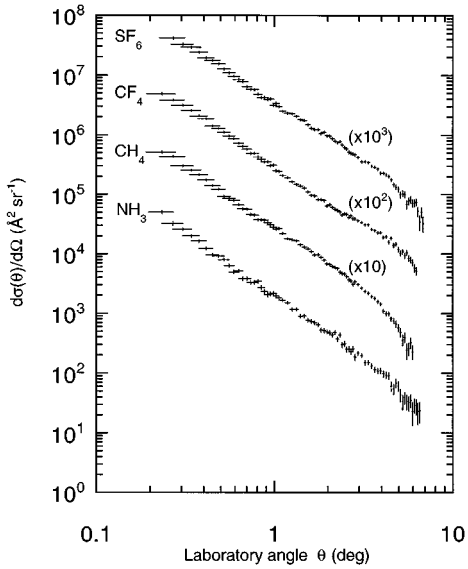

FIG. 5. Differential cross sections for elastic scattering of 0.5 keV O atoms by NH_3, CH_4, CF_4, and SF_6. The cross sections have been multiplied by the factors indicated.

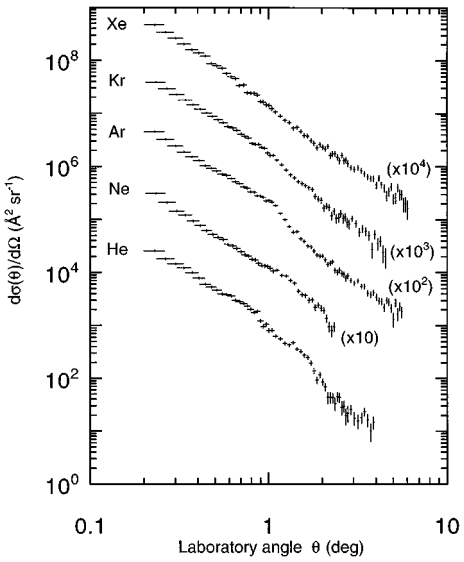

FIG. 6. Differential cross sections for elastic scattering of 1.5 keV O atoms by He, Ne, Ar, Kr, and Xe. The cross sections have been multiplied by the factors indicated.

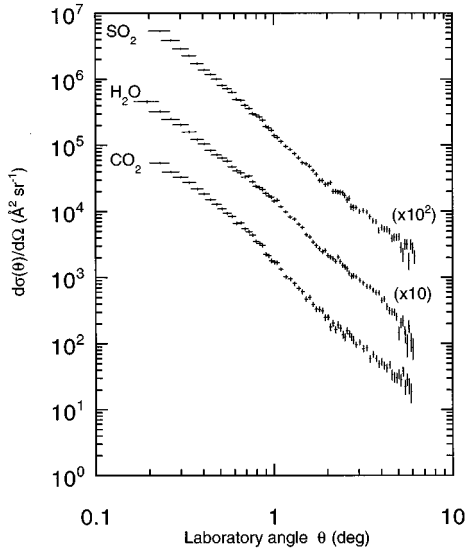

FIG. 8. Differential cross sections for elastic scattering of 1.5 keV O atoms by CO_2, H_2O, and SO_2. The cross sections have been multiplied by the factors indicated.

of the initiating particle. Deflection plates DP2 deflect charged-collision products away from the detector.

III. MEASURED QUANTITIES

Under thin target conditions, the differential cross section can be expressed as

$$\frac{d\sigma(\theta)}{d\Omega} = \frac{\Delta S(\theta)}{S_o \tau \Delta\Omega}, \tag{1}$$

where S_o is the primary beam flux, $\Delta S(\theta)$ is the flux scattered at an angle θ into the solid angle $\Delta\Omega$, and τ is the target thickness. Earlier studies in this laboratory [6] have demonstrated that the target thickness is accurately represented by the product of l the physical length of the cell and n the number density of the target gas that is obtained from a measurement of the target gas pressure using an MKS Baratron capacitance diaphragm gauge.

The signal on the PSD is first measured with no gas in the target cell. This measurement gives the extent of the area impacted by the primary beam and also includes contributions originating from intrinsic detector noise and from scattering by background gas and aperture edges. Target gas is next introduced and the signal is again recorded. The primary beam flux S_o is taken to be equal to the total number of counts detected, while the number recorded at detector locations that lie outside the area on which the primary beam is

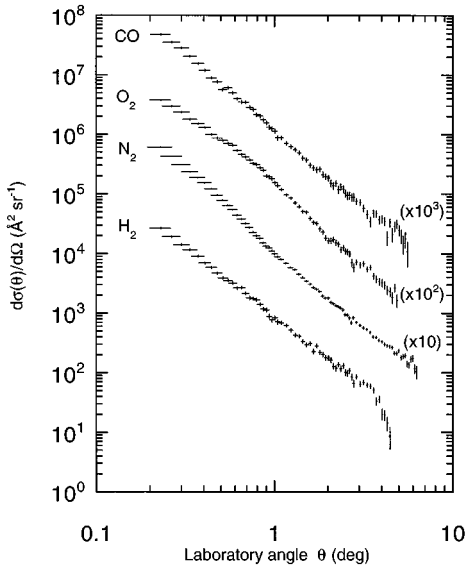

FIG. 7. Differential cross sections for elastic scattering of 1.5 keV O atoms by H_2, N_2, O_2, and CO. The cross sections have been multiplied by the factor indicated.

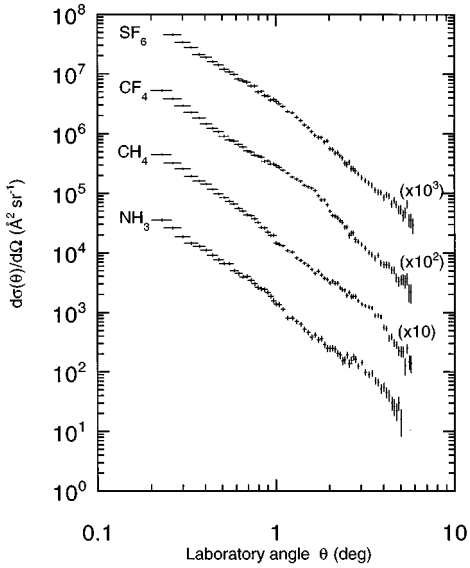

FIG. 9. Differential cross sections for elastic scattering of 1.5 keV O atoms by NH_3, CH_4, CF_4, and SF_6. The cross sections have been multiplied by the factors indicated.

TABLE II. Laboratory-frame differential elastic-scattering cross sections for 0.5-keV O-atom collisions. The numbers in square brackets represent powers of ten.

	$\frac{d\sigma(\theta)}{d\Omega}$(Å^2 sr^{-1})				
Laboratory angle θ (deg)	He	Ne	Ar	Kr	Xe
0.23±0.04	4.15±0.25 [4]	3.70±0.20 [4]	4.36±0.24 [4]	5.99±0.25 [4]	6.05±0.28 [4]
0.49±0.04	7.99±0.36 [3]	7.98±0.36 [3]	1.04±0.04 [4]	1.10±0.04 [4]	1.14±0.04 [4]
0.99±0.04	1.42±0.10 [3]	1.45±0.10 [3]	2.21±0.13 [3]	2.29±0.13 [3]	2.65±0.15 [3]
1.98±0.04	3.77±0.26 [2]	3.27±0.25 [2]	6.49±0.35 [2]	5.83±0.33 [2]	6.06±0.36 [2]
3.96±0.04	4.23±0.60 [1]	9.51±0.87 [1]	1.02±0.08 [2]	9.48±0.74 [1]	7.75±0.74 [1]
	H_2	N_2	O_2	CO	
0.23±0.04	4.65±0.25 [4]		3.99±0.22 [4]	5.30±0.22 [4]	
0.49±0.04	8.12±0.37 [3]	1.57±0.05 [4]	9.55±0.37 [3]	1.10±0.04 [4]	
0.99±0.04	1.36±0.10 [3]	2.92±0.14 [3]	2.15±0.12 [3]	2.69±0.14 [3]	
1.98±0.04	3.00±0.24 [2]	3.92±0.27 [2]	6.16±0.32 [2]	4.81±0.29 [2]	
3.96±0.04	5.90±0.67 [1]	4.56±0.61 [1]	6.36±0.68 [1]	5.95±0.65 [1]	
	CO_2	H_2O	SO_2		
0.23±0.04	5.31±0.23 [4]	4.02±0.21 [4]	7.34±0.36 [4]		
0.49±0.04	1.18±0.42 [4]	8.69±0.32 [3]	1.80±0.06 [4]		
0.99±0.04	3.17±0.15 [3]	1.78±0.10 [3]	3.25±0.17 [3]		
1.98±0.04	7.50±0.37 [2]	4.82±0.26 [2]	5.10±0.35 [2]		
3.96±0.04	9.63±0.80 [1]	9.66±0.71 [1]	8.81±0.80 [1]		
	NH_3	CH_4	CF_4	SF_6	
0.23±0.04	5.00±0.35 [4]	5.11±0.28 [4]	4.85±0.25 [4]		
0.49±0.04	9.20±0.51 [3]	1.21±0.04 [4]	1.28±0.04 [4]	1.54±0.06 [4]	
0.99±0.04	2.15±0.17 [3]	2.81±0.14 [3]	3.09±0.15 [3]	3.18±0.17 [3]	
1.98±0.04	4.90±0.40 [2]	6.76±0.36 [2]	6.37±0.34 [2]	9.70±0.48 [2]	
3.96±0.04	1.10±0.12 [2]	1.43±0.09 [2]	2.26±0.11 [2]	2.27±0.12 [2]	

incident, after appropriate correction for background effects, gives $\Delta S(\theta)$. As all of the incident particles are of the same species and energy, and are collected on the same detector, it is not necessary to know the absolute detection efficiency of the PSD. It is sufficient to bias the detector so that the detection efficiencies of the high-flux-density primary beam and the relatively low-flux-density scattered signal are equal [10]. In all cases, particle impacts on the PSD are decoded into x and y coordinates and the appropriate elements in a 360×360 array are incremented, with each array element corresponding to a 65×65 μm area on the detector face. Organizing the two-dimensional array into concentric rings about the scattering center and summing the recorded events in each ring reveals the scattering signal as a function of scattering angle θ. The uncertainty in the number of counts at each scattering angle is primarily statistical, while factors contributing to the angular uncertainties include the finite width of the primary beam, the discrete nature of the analysis rings, and inherent electronic noise in the PSD's position decoding electronics. These uncertainties are shown as vertical and horizontal error bars in the differential cross section results, while other factors adding uncertainty to the measurements are summarized in Table I.

IV. EXPERIMENTAL RESULTS

Absolute differential cross sections (DCS's) for the direct scattering of atomic oxygen are shown in Figs. 2–9 and in most cases exhibit a featureless monotonic behavior. The values of these cross sections at selected angles are given in Tables II and III. The corresponding integral cross sections are listed in Table IV. A comparison with earlier O-atom direct scattering measurements [5] shows agreement within the stated error bars. While most of the DCS's measured are featureless, some structure is seen at the higher energy for the lighter rare gas targets. In these cases it is believed that inelastic processes leading to target and projectile excitation give rise to the structure through interference between different scattering amplitudes. While these same processes may also be occurring for the heavier atomic and complex molecular targets, the structure in these cases would tend to be much less distinct due to the large number and closer spacing of the contributing states. A notable observation regarding the DCS's is their close similarity to one another in both amplitude and angular dependence despite the wide variety of targets, from small atoms to large complex molecules. When the DCS's are compared in the center-of-mass refer-

TABLE III. Laboratory-frame differential elastic-scattering cross sections for 1.5 keV O-atom collisions. The numbers in square brackets represent powers of ten.

	$\frac{d\sigma(\theta)}{d\Omega}$(Å^2 sr^{-1})				
Laboratory angle θ (deg)	He	Ne	Ar	Kr	Xe
0.23±0.03	2.56±0.10 [4]		4.54±0.12 [4]		4.70±0.16 [4]
0.51±0.03	4.68±0.21 [3]	4.76±0.24 [3]	8.18±0.28 [3]	7.78±0.30 [3]	7.94±0.35 [3]
1.01±0.03	8.03±0.68 [2]	1.25±0.09 [3]	2.28±0.11 [3]	1.70±0.10 [2]	1.41±0.11 [3]
2.02±0.03	8.50±1.18 [1]	2.04±0.27 [2]	2.05±0.17 [2]	1.99±0.29 [2]	2.33±0.23 [2]
4.04±0.03	5.47±3.70 [0]		3.44±0.45 [1]	3.80±0.70 [1]	4.44±0.63 [1]
	H_2	N_2	O_2	CO	
0.23±0.03	2.65±0.10 [4]	5.99±0.06 [4]	3.76±0.12 [4]	4.77±0.15 [4]	
0.51±0.03	3.89±0.19 [3]	7.71±0.13 [3]	7.82±0.27 [3]	5.65±0.28 [3]	
1.01±0.03	8.31±0.68 [2]	9.76±0.33 [2]	1.53±0.09 [3]	1.13±0.09 [3]	
2.02±0.03	1.77±0.16 [2]	1.76±0.07 [2]	1.66±0.15 [2]	1.83±0.19 [2]	
4.04±0.03	2.04±0.42 [1]	3.27±0.02 [1]	3.26±0.46 [1]	3.78±0.54 [1]	
	CO_2	H_2O	SO_2		
0.23±0.03	5.42±0.16 [4]	3.24±0.10 [4]	5.36±0.13 [4]		
0.51±0.03	1.09±0.04 [4]	6.44±0.21 [3]	8.02±0.25 [3]		
1.01±0.03	1.69±0.12 [3]	1.43±0.07 [3]	1.40±0.08 [3]		
2.02±0.03	2.50±0.23 [2]	2.14±0.15 [2]	2.60±0.18 [2]		
4.04±0.03	5.29±0.61 [1]	4.48±0.39 [1]	5.68±0.50 [1]		
	NH_3	CH_4	CF_4	SF_6	
0.23±0.03	3.52±0.16 [4]	4.48±0.12 [4]	5.26±0.18 [4]		
0.51±0.03	6.60±0.35 [3]	8.50±0.29 [3]	9.04±0.34 [3]	1.21±0.05 [4]	
1.01±0.03	1.40±0.12 [3]	1.46±0.08 [3]	2.92±0.14 [3]	3.43±0.19 [3]	
2.02±0.03	2.47±0.29 [2]	3.12±0.20 [2]	4.97±0.30 [2]	5.61±0.39 [2]	
4.04±0.03	5.58±0.91 [1]	5.64±0.51 [1]	6.31±0.72 [1]	8.48±0.95 [1]	

ence frame it is observed that with few exceptions, the cross sections lie within approximately ±50% of a central average cross section throughout the entire angular range studied.

V. CROSS-SECTION EXTRAPOLATIONS

The measured differential cross sections for selected targets have been used to derive empirical interaction potential-energy curves using a single-channel Wentzel-Kramers-Brillouin (WKB) partial-wave method as described in previous publications [7,11]. The derived potentials are then used to extrapolate the cross sections to 0.1 keV (laboratory energy), where particle detection as well as primary beam intensity and stability considerations make direct measurements impractical with the present apparatus. For N_2, CO, and H_2O targets the analytic potential form

$$V_1(r)=A_1\frac{e^{-\alpha_1 r}}{r}+A_2e^{-\alpha_2 r} \tag{2}$$

provides an excellent fit to the measured data, while the CO_2 data require the greater flexibility of the form

$$V_2(r)=\sum_{n=-1}^{2} B_n e^{-\beta_n r} r^n. \tag{3}$$

Optimization of the potential parameters was performed through iterative comparisons between the calculated and measured cross sections using a nonlinear least-squares-fitting routine, yielding the parameters listed in Table V. In all of the cases shown in Table V a single set of parameters was used to fit the scattering data for a given pair of reactants at both 0.5 and 1.5 keV simultaneously. This suggests that these processes contain negligible contributions from inelastic scattering. Previous experience using this fitting technique [11] showed that as inelastic processes become more significant at higher collision energies it is not always possible to fit data at different energies with a single potential. An example of the quality of the fits achieved with the present data is shown in Fig. 10.

In calculating differential cross sections from a derived potential, only a limited region of the potential is important. This is a consequence of the fact that the scattering behavior is very sensitive to features of the potential near the classical turning points, where the relative motion of the reactants is at

TABLE IV. Integral direct-scattering cross sections.

Target	O (0.5 keV) Angular range (deg)	O (0.5 keV) Cross section (Å^2)	O (1.5 keV) Angular range (deg)	O (1.5 keV) Cross section (Å^2)
He	0.20–6.27	10.4	0.20–4.04	5.6
Ne	0.20–6.27	10.7	0.20–2.48	6.3
Ar	0.20–6.27	15.1	0.20–6.16	10.8
Kr	0.20–6.27	16.2	0.20–6.12	10.1
Xe	0.20–6.27	16.2	0.20–6.16	10.3
H_2	0.20–6.27	11.1	0.20–4.88	6.0
N_2	0.20–6.27	15.5	0.20–6.13	10.1
O_2	0.20–6.27	14.2	0.20–6.16	9.6
CO	0.20–6.27	14.6	0.20–6.16	9.1
CO_2	0.20–6.27	17.9	0.20–6.16	12.9
H_2O	0.20–6.27	12.2	0.20–6.16	8.8
SO_2	0.20–6.27	19.8	0.20–6.16	11.6
NH_3	0.20–6.27	13.6	0.20–6.16	9.2
CH_4	0.20–6.27	17.9	0.20–6.16	11.9
CF_4	0.20–6.27	19.8	0.20–6.16	15.3
SF_6	0.20–6.27	22.8	0.20–6.16	18.3

a minimum and thus the time available for action of the forces corresponding to the potential is longest [12]. Therefore, the pertinent region of the potential is that which includes the classical turning points of all relevant trajectories. This region is defined by the classical turning points corresponding to the smallest angle at the lowest energy and the largest angle at the highest energy. Classically speaking, the measurements yield no information about the potential at internuclear separations smaller than the smallest turning point. Therefore, great care must be taken if the derived potentials are to be used to extrapolate the measured cross sections at a given energy to larger angles. Similarly it is found that the calculated cross sections are largely insensitive to changes in the potential at separations larger than the largest turning point; thus, the accuracy of the derived potentials in this region is considered both uncertain and unimportant. For these reasons the extrapolations to 0.1 keV are performed using the potentials only over the ranges defined by the turning points whose values are shown in Table V. The calcu-

TABLE V. Interaction potential parameters. The range over which each potential is valid ($r_{\min}$–$r_{\max}$) is defined by the classical turning points as discussed in the text.

Screened Coulomb plus exponential form: $V_1(r)=A_1\frac{e^{-\alpha_1 r}}{r}+A_2e^{-\alpha_2 r}$			
Parameter	O+N_2	O+CO	O+H_2O
A_1 (eV Å)	1.43×10^7	7.56×10^7	5.04×10^{12}
α_1(Å^{-1})	10.69	13.52	16.49
A_2 (eV)	256	403	1.68×10^4
α_2(Å^{-1})	2.357	2.728	4.169
Valid range:			
$r_{\min}$–$r_{\max}$(Å)	1.19–2.38	1.08–2.24	1.56–2.42
Modified Cerperley and Partridge form: $V_2(r)=\sum_{n=-1}^{2}B_ne^{-\beta_n r}r^n$			
Parameter	O + CO_2		
B_{-1} (eV Å)	8.21×10^5		
β_{-1}(Å^{-1})	7.785		
B_0 (eV)	-1.35×10^4		
β_0(Å^{-1})	4.335		
B_1 (eV Å^{-1})	4.95×10^3		
$\beta_{1,2}$(Å^{-1})	3.939		
B_2 (eV Å^{-2})	1.46×10^3		
Valid range:			
$r_{\min}$–$r_{\max}$(Å)	1.19–2.58		

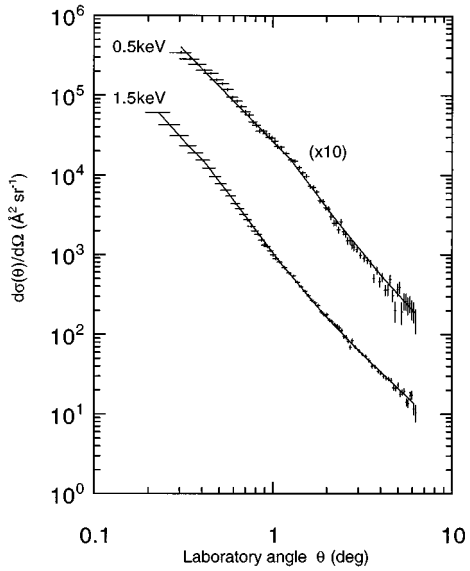

FIG. 10. Differential cross sections for O+N_2 elastic scattering. The solid line is a fit to the experimental data using the $V_1(r)$ potential form. The cross sections have been multiplied by the factors indicated.

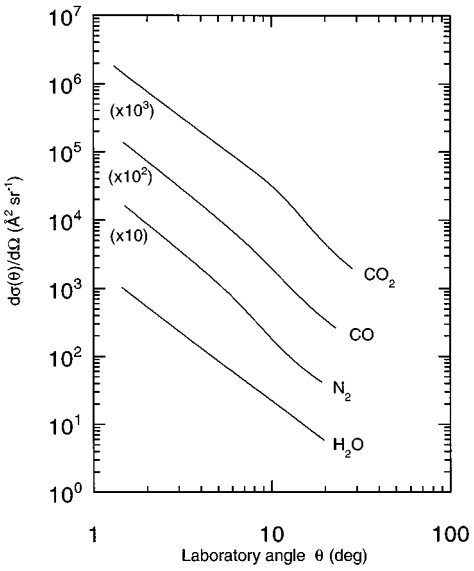

FIG. 11. Calculated differential cross sections for elastic scattering of 0.1 keV O atoms by CO_2, CO, N_2, and H_2O. The cross sections have been multiplied by the factors indicated.

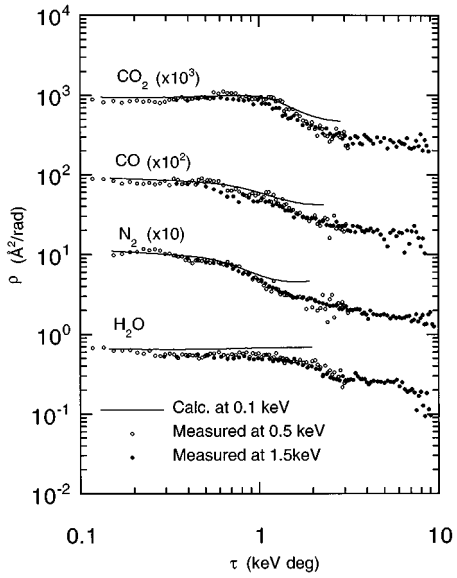

FIG. 12. Comparison, in reduced coordinates, of the differential cross sections for O-atom elastic scattering calculated at 0.1 keV and the experimental data at 0.5 and 1.5 keV. The cross sections have been multiplied by the factors indicated.

lated differential cross sections for N_2, CO, CO_2, and H_2O targets are shown in Fig. 11.

An interesting observation made during this analysis was the nonuniqueness of the potentials as described by Newton [13]. Using the V_1 potential form, fits to the N_2, CO, and H_2O measurements reveal from two to three distinctly different potentials for each target, each yielding nearly indistinguishable calculated cross sections at all three of the energies studied. Although it is possible that, for each target, more such potentials may exist than those that were found, efforts to find a large family of such potential curves, either continuous or discrete, were unsuccessful. In these efforts, the potentials being refined invariably converged to one of the potentials already found. It is reasonable then to consider the potentials found as corresponding to several distinct local minima in the fourfold parameter space of the fit. Recall that although the idealized single-channel scattering calculations performed here seem to mandate a unique physical potential, the potentials actually used are empirical rather than physical and are presumed to represent contributions from many contributing molecular states and target orientations.

Since the measurements used to extrapolate to lower energy may include contributions from inelastic processes, it is necessary to investigate the accuracy of the calculated cross sections. A good indicator of this accuracy is a comparison in reduced coordinates $\tau = E\theta$ and $\rho = \theta \sin(\theta) d\sigma/d\Omega$ as described by Smith, Marchi, and Dedrick [14], a method which has been used extensively in the past for analyzing collision cross sections. In these coordinates it can be shown that if the collision energy is much larger than the interaction energy between the particles and if the scattering is from a single, repulsive potential, then for each value of τ there is a unique value of ρ. Thus data taken at different energies but plotted in τ, ρ coordinates should fall on a single curve. However, as this approach is based on an approximation to a series expansion, at some point as τ increases the approximation will no longer be valid and data taken at different energies will inevitably diverge. A comparison between the measured and the calculated cross sections in reduced coordinates for the targets studied is presented in Fig. 12 and shows excellent agreement at small τ values. At larger τ values, the expected divergence seen in the 0.1 keV data corresponds to laboratory scattering angles as large as $10°-15°$. This favorable comparison, along with the lack of difficulty in fitting multiple-energy data with single sets of parameters, suggests that contributions to the cross sections from inelastic processes are not significant for collisions of O atoms with the four targets studied here.

ACKNOWLEDGMENTS

This work was supported by the Robert A Welch Foundation and the National Science Foundation, Atmospheric Sciences Section.

[1] E. G. Shelley, R. G. Johnson, and R. D. Sharp, J. Geophys. Res. **77**, 6104 (1972).

[2] R. D. Sharp, R. G. Johnson, and E. G. Shelley, J. Geophys. Res. **81**, 3283 (1976).

[3] M. R. Torr, J. C. G. Walker, and D. G. Torr, J. Geophys. Res. **79**, 5267 (1974).

[4] E. Unterreiter and H. Winter, in *The Seventeenth International Conference on the Physics of Electronic and Atomic Collisions, Abstracts of Contributed Papers, Brisbane, Australia*, edited by W. R. MacGillivray, I. E. McCarthy, and M. C. Standage (AIP, New York, 1992).

[5] D. A. Schafer, J. H. Newman, K. A. Smith, and R. F. Steb-

bings, J. Geophys. Res. **92**, 6107 (1987).
[6] J. H. Newman, K. A. Smith, and R. F. Stebbings, J. Geophys. Res. **90**, 11 045 (1985).
[7] D. E. Nitz, R. S. Gao, L. K. Johnson, K. A. Smith, and R. F. Stebbings, Phys. Rev. A **35**, 4541 (1987).
[8] R. F. Stebbings, B. R. Turner, and J. A. Rutherford, J. Geophys. Res. **71**, 771 (1966).
[9] T. F. Moran and J. B. Wilcox, J. Chem. Phys. **69**, 1397 (1978).
[10] R. S. Gao, P. S. Gibner, J. H. Newman, K. A. Smith, and R. F. Stebbings, Rev. Sci. Instrum. **55**, 1756 (1984).
[11] R. S. Gao, L. K. Johnson, K. A. Smith, and R. F. Stebbings, Phys. Rev. A **40**, 4914 (1989).
[12] F. T. Smith, R. P. Marchi, W. Aberth, and D. C. Lorents, Phys. Rev. **161**, 31 (1967).
[13] R. G. Newton, J. Math. Phys. **3**, 75 (1962).
[14] F. T. Smith, R. P. Marchi, and K. G. Dedrick, Phys. Rev. **150**, 79 (1966).